Published in final edited form as:

Nat Nanotechnol. 2022 June ; 17(6): 653–660. doi:10.1038/s41565-022-01130-3.

In vivo Non-Invasive Confocal Fluorescence Imaging Beyond 1700 nm Using Superconducting Nanowire Single-Photon Detectors

Feifei Wang[1,†],

Fuqiang Ren[1,†],

Zhuoran Ma[1,†],

Liangqiong Qu[2],

Ronan Gourgues[3],

Chun Xu[1],

Ani Baghdasaryan[1],

Jiachen Li[1],

Iman Esmaeil Zadeh[4],

Johannes WN Los[3],

Andreas Fognini[3],

Jessie Qin-Dregely[3],

Hongjie Dai[1,*]

[1] Department of Chemistry and Bio-X, Stanford University, Stanford, CA 94305, USA.

[2] School of Medicine, Stanford University, Stanford, CA 94303, USA.

[3] Single Quantum B.V., Delft 2628 CJ, The Netherlands

[4] Department of Imaging Physics, Delft University of Technology, Delft 2628 CJ, The Netherlands.

Abstract

Light scattering by biological tissues sets a limit to the penetration depth of high-resolution optical microscopy imaging of live mammals in vivo. An effective approach to reduce light scattering and increase imaging depth is by extending the excitation and emission wavelengths to the > 1000 nm second near-infrared (NIR-II), also called the short-wavelength infrared (SWIR) window. Here, we show biocompatible core-shell lead sulfide/cadmium sulfide (PbS/CdS) quantum dots

* Correspondence to: hdai@stanford.edu.

† These authors contribute equally to this work.

Author contributions

H.D. and F.W. conceived and designed the experiments. H.D. and F.W. designed the optical system. F.W. set up the optical system. F.W., F.R. and Z.M. performed the experiments. F.R. synthesize the PbS/CdS QD. R.G., I.E.Z., J.W.L., A.F. and J.Q.D. developed the SNSPD optimized in 1550-2000 nm window. F.W., F.R., Z.M., L.Q., C.X., A.B., J.L. and H.D. analyzed the data. F.W. and H.D. wrote the manuscript. All authors contributed to the general discussion and revision of the manuscript.

Competing interests

The authors declare the following financial competing interests: the following authors were employed by Single Quantum and may profit financially: R.G., J.W.L., A.F., and J.Q.D.

emitting at ~1880 nm and superconducting nanowire single photon detectors (SNSPD) for single-photon detection up to 2000 nm, enabling one-photon excitation fluorescence imaging window in the 1700–2000 nm (NIR-IIc) range with 1650 nm excitation, the longest one-photon excitation and emission for in vivo mouse imaging to date. Confocal fluorescence imaging in NIR-IIc reached an imaging depth of ~ 1100 μm through intact mouse head, and enabled non-invasive cellular-resolution imaging in the inguinal lymph nodes (LNs) of mice without any surgery. We achieve In vivo molecular imaging of high endothelial venules (HEVs) with diameter down to ~ 6.6 μm and CD169+ macrophages and CD3+ T cells in the lymph nodes, opening the possibility of non-invasive intravital imaging of immune trafficking in lymph nodes at the single-cell/vessel level longitudinally.

In vivo high resolution optical microscopic imaging of mice has empowered investigations of biological structures, molecular nature/identity of cell surface receptors and cellular processes, events and functions at the single-cell level. However, the heterogeneous nature and complex compositions of biological tissues present a major challenge, limiting the imaging penetration and signal to background ratios (SBR) due to light scattering and endogenous tissue autofluorescence. Extending the excitation wavelength to the NIR and SWIR (900–3000 nm) range by multi-photon (MP) imaging has been highly successful in suppressing scattering and affording greater penetration depths, but still relies on invasive surgery to expose underlying organs such as the brain and lymph nodes in order to afford sufficient imaging depths and resolution [1–6]. Up to 1700 nm excitation has been employed by three-photon microscopy[7], enabling > 500 μm deep through-skull (with scalp removed) mouse brain 3D volumetric imaging[8].

In recent years various fluorescent/luminescence dyes and nanoparticle probes with emission in the 1000–1700 nm range have been developed, including small organic molecules[9,10], carbon nanotubes (CNTs)[11], quantum dots[12,13] and rare-earth nanoparticles[14–16]. Using these dyes and probes confocal[12,17] and light-sheet microscopy (LSM)[18,19] employed one-photon excitation up to 1540 nm and emission up to 1700 nm to benefit from reduced scattering of both excitation and emission light[19], affording non-invasive in vivo microscopy of blood micro-vessels and molecular imaging at single-cell level. In vivo NIR-II microscopy imaging has facilitated investigating mouse models of cardiovascular diseases, brain injury and cancer, as exemplified by imaging of CD4, CD8, OX40 and other bio-markers on immune cells in the tumor microenvironment in response to immunotherapy[12,18–20].

One of the limiting factors of optical imaging depth into biological tissues is water absorption[21] that exhibits a local peak at ~ 1445 nm due to the vibrational overtone mode of O-H bond bending (Fig. 1a, and Supplementary Fig. 1). In the 800–1400 nm range (including the previously defined NIR-IIa sub-window of 1300–1400 nm)[22] light absorption is relatively low and imaging depths in tissues such as the brain are dominant by scattering (Fig. 1b). It is possible to image at centimeter depth but with the loss of resolution due to light scattering (Fig. 1b).[23] Both absorption and scattering influence NIR-IIb (defined as 1500–1700 nm)[24] imaging depth in mouse brain, with an effective attenuation length[1] of $l_e = 1/(1/l_s+1/l_a)$, where l_s is the scattering length in mouse brain and can be mimicked

by 5% intralipid[18]. l_a is the attenuation length of light due to water absorption (Fig. 1b). The NIR-IIb sub-window affords a longer attenuation length l_e than in 1000–1400 nm due to reduced light scattering (Fig.1b), allowing for deeper imaging. The 1700 nm NIR-IIb border-line is set by the upper detection limit of indium gallium arsenide (InGaAs) detectors (900–1700 nm) commonly used for NIR-II/SWIR imaging. Beyond 1700 nm, light scattering further reduces but water adsorption increases (Fig.1a,b). Here we define the 1700–2000 nm as the NIR-IIc sub-window and revised the NIR-II window to be 1000–3000 nm (with the upper bound being the same as SWIR[25]). Also, the final sub-window in NIR-II/SWIR for one-photon excitation imaging would be ~ 2100–2300 nm (defined here as the NIR-IId sub-window) range with similar attenuation length as NIR-IIc (Fig. 1b), beyond which water absorption becomes overwhelming and through-tissue fluorescence imaging is impossible (Fig. 1a). Thus far there has been no report of fluorescence imaging by one-photon excitation of living systems in the > 1700 nm range, limited by the lack of biocompatible fluorescent/luminescent probes with sufficient quantum yield/brightness, and that InGaAs cameras/detectors are insensitive to light > 1700 nm in the NIR-IIc/NIR-IId range.

Here we developed aqueous soluble core-shell lead sulfide/cadmium sulfide quantum dots (PbS/CdS QD) with emission peak ~ 1880 nm and employed superconducting nanowire single photon detectors (SNSPD) for in vivo imaging in the > 1700 nm range to further suppress light scattering and push the limit of one-photon excited through-tissue imaging. Confocal microscopy through mouse tissues in the NIR-IIc window revealed mouse scalp/skull/brain structures in 3D and enabled surgery-free molecular imaging of the peripheral node addressin (PNAd) on HEVs, and CD169+ macrophages and CD3+ T cells inside mouse inguinal lymph nodes non-invasively.

Quantum dots and SNSPD for NIR-IIc imaging

We synthesized PbS quantum dots with emission peak at ~ 2009 nm via a modified organometallic route[26]. A CdS shell on the PbS core was then grown by the cation exchange approach to protect the PbS core from degradation[12]. The shell growth step shifted the emission peak of the core to ~ 1880 nm (Supplementary Fig. 2a, see synthesis procedure in Methods). The resulting PbS/CdS QD with emission peak in NIR-IIc (named ‘QDc’ herein) showed a narrow size distribution around ~ 8 nm (Fig. 1c and Supplementary Fig. 2b), larger than our previous ~ 6.9 nm QD with emission peak in NIR-IIb (named ‘QDb’)[12]. To transfer the QDc from organic phase to aqueous phase, a hydrophilic polymeric cross-linked network (P^3 coating) developed by our group was coated on the QDc to impart biocompatibility in physiological environments and biliary excretion in ~ 2 weeks without apparent toxic effects[14,27]. The final aqueous stabilized P^3-QDc exhibited a peak emission wavelength of ~ 1820 nm in NIR-IIc (Fig. 1d). Dynamic light scattering (DLS) analysis of the P^3-QDc showed an average hydrodynamic size of ~ 32 nm in aqueous solutions (Fig. 1e).

The upper spectral detection limit of 1700 nm for InGaAs detectors was overcome by SNSPD designed for wavelengths from 1550 nm to 2000 nm (Fig. 1f,g). The single-photon detectors were fabricated on an optimized niobium titanium nitride (NbTiN) superconducting film[28] with an optimized superconducting nanowire width and detector

geometry (see Supplementary Note 1 for details of the SNSPD). The SNSPD were connected to our home-built confocal microscope through single mode (SM) fibers transmitting in 1200–2000 nm (see Methods and Supplementary Figs. 3 and 4) allowing diffraction-limited resolution in non-scattering media (see resolution analysis in Methods).

Phantom imaging in NIR-IIb and NIR-IIc sub-windows

We first imaged a 50 μm diameter capillary filled with aqueous suspensions of P^3-QDb or P^3-QDc with emission peak residing in NIR-IIb (1500–1700 nm)[12] or NIR-IIc (1700–2000 nm) immersed in ~ 5% intralipid solution, mimicking blood vessels in a mouse brain tissue (Fig. 2a–c). NIR-IIc fluorescence was collected in 1800–2000 nm (see Method for filters used), but at millimeters imaging depths the actual upper limit was ~ 1900 nm set by water absorption (Fig.1a). This was also gleaned by that the detected fluorescence signals of QDc through 2–10 mm thick layers of water showed diminished > 1900 nm signals due to water absorption (Fig. 2d), while emission was clearly detected in the 1600–1850 nm range even through a 10 mm thick water layer. We set the upper limit of NIR-IIc as 2000 nm since the 1850–2000 nm emission could still be detected for imaging shallower layer of tissues in vivo. For wide-field imaging of QDb filled capillary in the 1500–1700 nm range of NIR-IIb with an InGaAs camera (excitation: 808 nm), the capillary was resolved at up to ~ 3.2 mm immersion depth in the intralipid solution with a SBR of 1.28 but the SBR was low, ~ 1 at 4.4 mm depth (Fig. 2a, first column and Supplementary Fig. 5). Confocal microscopy (with a 10X objective, z resolution ~ 18 μm) imaging in the same 1500–1700 nm range using the SNSPD (under 1319 nm laser excitation) afforded improved SBR over InGaAs camera imaging as imaging depth < 2.3 mm (Fig. 2c), but was incapable of resolving the capillary beyond ~ 2.6 mm depth (Fig. 2a, second column). The ‘sidelobes’ around the capillary in the wide-field images were attributed to scattered light and can be rejected by the confocal microscopy (Fig. 2a) but with the sacrifice in temporal resolution due to raster scanning required. Wide-field imaging is advantageous in simplicity and fast imaging. Confocal microscopy (1800–2000 nm emission; 1540 nm excitation) imaging of QDc filled capillary in NIR-IIc using the SNSPD extended the imaging depth to ~ 3.2 mm (Fig. 2a, third column). When a 1650 nm laser was used for NIR-IIc excitation, the highest SBR was achieved at all depths (Fig. 2c) and the capillary was resolved at up to ~ 4.4 mm (Fig. 2a, forth column), deeper than NIR-IIc imaging under 1540 nm excitation and NIR-IIb imaging under 1319 nm excitation.

Monte Carlo simulations [29] observed light spreading laterally (along x) and intensity decaying longitudinally (along z) due to tissue absorption and scattering through a tissue mimicking medium (Supplementary Fig. 6a), and the spreading effect reduced for longer wavelength light (Supplementary Fig. 6b). Compared to a 1319 nm laser, a 1540 nm laser experienced less scattering but decayed faster due to ~ 4.4 times higher absorption than the 1319 nm laser (Fig. 1a). Due to the combined absorption and scattering effects, the 1650 nm laser transmitting through a turbid medium showed the lowest decay in intensity and the least beam broadening than other wavelength lasers (800 nm, 1000 nm, 1319 nm and 1540 nm, Supplementary Fig. 6), which was ideal for NIR-IIc imaging to optimize the penetration depths of both the excitation and emission light through biological tissues.

Intact mouse head imaging in NIR-IIb and NIR-IIc sub-windows

Upon tail-vein injection of P^3-QDc, we performed NIR-IIc non-invasive 3D confocal imaging of blood vessels through intact mouse head (Fig. 3a,b). The circulating P^3-QDc labeled blood vessels in intact mouse head layers including scalp, skull, meninges and ~ 550 μm or ~ 900 μm thick brain cortex were resolved by 3D volumetric NIR-IIc imaging, at depth up to ~ 800 μm or 1100 μm under 1540 nm or 1650 nm laser excitations respectively (Fig. 3b and Supplementary Video 1 for 3D views). Vessel like channels through the meninges connecting the skull and brain cortex were observed (Fig.3b, pointed by arrows). These vessels/channels were shown important to immune responses of the brain to injuries and infections[30].

Note that both NIR-IIc confocal microscopy and NIR-IIb LSM[18] can reject scattered and out-focus light enabling high contrast 3D imaging of mouse head. NIR-II LSM allowed faster imaging speed using wide-field detection, but the spectral detection range was < 1700 nm with InGaAs cameras, limiting the imaging depth for resolving small features in mouse brain. Through intact mouse head, the NIR-IIb LSM under 1319 nm excitation reached ~ 250 μm depth in the cortex[18], while NIR-IIc confocal imaging under 1650 nm excitation reach ~ 900 μm depth in the cortex.

We compared SNSPD to a commercial 900–1700 nm photomultiplier tube (PMT) for non-invasive confocal microscopy imaging through intact mouse head. A mouse was intravenously injected with P^3-QDb and P^3-QDc sequentially 30 min before imaging and excited by 1319 nm, 1540 nm, 1650 nm lasers respectively with the same power (28.5 mW at head surface, see power analysis in Supplementary Note 2, detailed experimental conditions are summarized in Supplementary Table 1). For NIR-IIb imaging under the same 1319 nm laser excitation, the SNSPD based confocal microscopy resolved small capillary vessels not detected by PMT and allowed higher spatial resolution at greater imaging depths (Fig. 3c first column for PMT vs. second column for SNSPD, and Fig. 3d). Under a laser excitation of 1540 nm, imaging in the NIR-IIc window afforded better resolution than in the NIR-IIb region under an excitation of 1319 nm, using the same SNSPD (Fig. 3c, second column, third column and Fig. 3d). Then we compared a 1650 nm laser to the 1540 nm laser for NIR-IIc imaging using the same SNSPD. 1650 nm excitation showed apparent improvement on resolution quantified by FWHM of features, SBR and penetration depth (Fig. 3c, third column, forth column, Fig. 3d,e). The wider broadening of point spread function (PSF) at shorter wavelength was evaluated by the blurred edges of blood vessels[8]. The full width at half maximum (FWHM) of a vessel imaged at z = 400 μm was measured to be 6.2 μm, 5.3 μm and 3.4 μm by SNSPD based confocal microscopy using 1319 nm, 1540 nm and 1650 nm lasers for NIR-IIb or NIR-IIc imaging, respectively (Fig. 3d left), suggesting increased spatial resolution. As the imaging depth increased to 700 μm, vessels not resolved by PMT were resolved in NIR-IIb and NIR-IIc widows by using SNSPD (Fig. 3c). Only the 1650 nm laser exited NIR-IIc imaging allowed imaging beyond the 1100 μm depth into the mouse head. Confocal microscopy in NIR-IIc window at 1650 nm excitation afforded the highest contrast, with a SBR of ~ 170 at z = 400 μm that decreased to ~ 5 at 1100 μm, which was ~ 3.3 times, ~ 3.3 times and ~ 11.5 times higher than NIR-IIc imaging at 1540 nm excitation, and NIR-IIb imaging with SNSPD and PMT respectively (Fig. 3e).

To assess the fastest scan rate possible by our current NIR-IIc confocal microscopy with 1650 nm excitation with various powers, we performed blood vessel imaging in mouse brain ex vivo. A scan rate of ~ 3 Hz (pixels: 133 × 200, scan area: 185 μm x 278 μm) was achieved down to 0.67 mW (Supplementary Fig. 7) and limited by the galvo mirror scan rate (~ 600 Hz at this scan area and pixels) and probe brightness.

Non-invasive in vivo NIR-IIc confocal microscopy of mouse inguinal lymph nodes

The lymphatic system plays crucial roles in immune responses to infections, cancer and vaccination. It is highly desirable to image and monitor cellular immunological events within the lymph nodes (LNs) in real-time and over-time longitudinally with cellular resolution. Here we imaged LNs though intact mouse skin, which differed from previous intravital microscopy with installed transparent windows by invasive surgery[4,31,32].

We first performed non-invasive in vivo NIR-IIc molecular imaging of the PNAd on high endothelial venules (HEVs) in inguinal lymph nodes (iLN) of mice (Fig. 4a–e). We conjugated anti-MECA-79 antibodies to P^3-QDc (aMECA-79-QDc), intravenously injected into a mouse through the tail-vein, and 24 h later injected an organic probe p-FE (excitation: 808 nm; emission: 1200–1400 nm)[20] as a blood vessel NIR-II imaging agent. The MECA-79 antibody was known to specifically target the 6-sulfo sialyl Lewis X epitope on PNAd expressed on HEV[33]. Ten minutes after injection of p-FE, we first performed wide-field imaging in NIR-IIb (the QDc exhibited emission in both NIR-IIb and NIR-IIc) and observed anti-MECA-79 targeted QDc emission in the iLN, with blood vessels labeled by circulating p-FE imaged in the 1200–1400 nm emission range (Fig. 4b, Fig. 4c left). In comparison, no QDc emission signal was detected in the iLN in control mice injected with free P^3-QDc without anti-MECA-79 conjugation (Supplementary Fig. 8a). Free P^3-QDc cleared from the liver faster than the aMECA-79-QDc (Supplementary Fig. 8a–c). This could be that normal liver are known to over-express MECA-79 sulfated glycans[34], leading to stronger signal and longer retention of aMECA-79-QDc in the liver. To further confirm specific targeting of aMECA-79-QDc to HEVs, we injected free MECA-79 antibodies 24 h before aMECA-79-QDc injection as a blocking experiment. In another control, we injected TRC105-QDc intravenously (TRC105 is an irrelevant antibody to PNAd; it targets endoglin overexpressed on proliferating endothelial cells[35]). In both cases we did not observe apparent NIR-IIc signal in the iLN (Supplementary Fig. 8d,e), confirming specific molecular targeting of HEVs in LNs with aMECA-79-QDc injected intravenously.

Next we mapped out/differentiated the spatial distributions of blood vessels (with circulating p-FE dye) and HEVs (aMECA-79-QDc) in the iLN. At low magnifications the iLN region was imaged by both InGaAs wide-field system and SNSPD confocal microscopy (Fig. 4c). The latter clearly rejected scattering induced background and allowed weak signal detection in both 1200–1400 nm and NIR-IIc window. High-resolution 3D confocal imaging revealed HEVs in the iLN below a skin layer with p-FE labeling the skin blood vessels (Fig. 4d, Supplementary Figs. 9 and 10). Confocal imaging at different depths in vivo and ex vivo showed that only HEVs were labelled by aMECA-79-QDc, while both HEVs and

the surrounding blood vessels in the iLN were labeled by p-FE (Fig. 4d, Supplementary Figs. 9 and 10), confirming specific targeting of HEVs by aMECA-79-QDc. Confocal microscopy in NIR-IIc with 1540 nm excitation (Supplementary Fig. 9) or 1650 nm excitation (Supplementary Figs. 10) allowed iLN molecular imaging with a penetration depth of ~ 500 μm including the skin layer, which was ~ 2 X deeper than in imaging in the 1200–1400 nm range. The penetration depth for 1540 nm or 1650 nm excitations were similar because the size of iLN in z was ~ 500 μm but lower power was required by 1650 nm excitation (35 mW vs. 1.6–10.0 mW). The stability of P^3-QDc and the aMECA-79-QDc afforded lasting targeting effect, allowing for non-invasive NIR-IIc confocal microscopy imaging of HEVs in iLN longitudinally over more than 4 days (Fig. 4e).

Toward non-invasive in vivo NIR-IIc confocal microscopy imaging with cellular resolution in vivo, we performed two-color molecular imaging of CD169 (expressed on subcapsular-sinus macrophages) and CD3 (on T cells) in intact mouse iLN. We conjugated CD169 antibodies to quantum dots with peak emission at 1110 nm (aCD169-QDa) and CD3 antibodies to P^3-QDc (aCD3-QDc) and subcutaneously injected at the base of tail sequentially. One day post injection, wide-field images showed strong signals of aCD169-QDa and aCD3-QDc in iLN (Fig. 4f). Two color large area confocal microscopy (Fig. 4g,h) revealed CD169+ macrophages labelled by aCD169-QDa outlining the subcapsular sinus; with CD3+ T cells in the T cell zone in interior of the lymph node labeled by aCD3-QDc. Unlabeled B cell follicles were also recognizable (dark regions in Fig. 4h) as they were close to the layer of macrophages and surrounded by T cells[36,37]. High-resolution confocal microscopy imaging of CD3+ T cells in NIR-IIc window with 1650 nm excitation resolved T cells labeled on the outside of the cells (dark in the middle) as deep as 500 μm in the intact iLN (Fig. 4i). Ex vivo, we stained cell nuclei with DRAQ7 dye (see Methods). Ex vivo confocal microscopy of DRAQ7 and aCD3-QDc (Fig, 4j) clearly resolved T cells outlined by aCD3-QDc with DRAQ7 labels inside the nuclei. These results established non-invasive NIR-IIc confocal microscopy imaging with cellular resolution in intact lymph nodes in vivo.

Conclusions

NIR-IIc confocal microscopy with single photon detectors afforded non-invasive cellular-resolution imaging through intact mouse head and lymph nodes longitudinally. Our one-photon excitation NIR-IIc confocal microscopy employed 1650 nm excitation, close to the longest excitation wavelength of ~1700 nm used for two-photon or three-photon microscopy[1,7]. These similar excitation lights undergo similar decay when transmitting through the thickness z of a tissue. However, while fluorescence emission in one-photon excitation microscopy scales linearly with light intensity $I(z)$, two-photon and three-photon fluorescence are nonlinear, scaling with the second and third power of the excitation light respectively, decay more rapidly than the one-photon case[38]. NIR-IIc confocal microscopy provides an alternative method to multiphoton microscopy at a lower cost (Supplementary Table 2). Integrating NIR-IIc confocal microscopy and multiphoton microscopy with ~ 1650–1700 nm excitation could be novel, allowing multi-channel imaging of complex biological systems using a broader range of probes. In terms of laser safety, we note that all ~ 60 mice used for in vivo imaging through this work were safe and healthy post imaging, without signs of skin burns (redness, scars, etc.) due to laser illumination. None of the

mice showed any abnormal behavior or signs of pain and discomfort after imaging. None of the mice had to be sacrificed after imaging. Further, we employed an approach of linearly increasing the laser power at increasing tissue depth to stay below the 1 J/cm^2 laser safety limit of 1650 nm laser (American National Standard for Safe Use of Lasers, ANSI Z136.1) while maximizing imaging signal (Supplementary Note 2). It is also important to note that the laser power/fluence needed for imaging depends on the brightness of the dyes/probes used. Although our current QDc are sufficiently bright for in vivo imaging within the safety limit, new advances in probe development could allow safe imaging much below the 1 J/cm^2 limit.

Methods

Materials

Lead (II) chloride ($PbCl_2$), 1-Octadecene (ODE), cadmium oxide (CdO) and sulfur powder (sublimed) were purchased from Alfa Aesar. Oleylamine, oleic acid, 1-octadecene, poly(maleic anhydride-alt-1-octadecene) (PMH; average molecular weight: 30k-50k), 4-morpholineethanesulfonic acid (MES), 4-(dimethylamino)pyridine (DMAP), poly(acrylic acid) (PAA; average molecular weight: 1800), 1-(3-dimethylaminopropyl)-3-ethylcarbodiimide hydrochloride (EDC), and 2-Amino-2-(hydroxymethyl)-1,3-propanediol (tris-base) were purchased from Sigma-Aldrich. Hexane, toluene, chloroform, and DI water were purchased from Fisher Scientific. Methoxy polyethylene glycol amine (mPEG-NH_2; average molecular weight: 5 kD) was purchased from Laysan-Bio. 8-arm polyethylene glycol amine (8Arm-PEG-NH_2·HCl; average molecular weight: 40 kDa) was purchased from Advanced Biochemicals. All the chemicals were used without further purification. 50 μm capillaries were bought from VitroCom. Purified anti-mouse/human PNAd antibody (Clone: MECA-79), purified anti-mouse CD169 antibody (Clone: 3D6.112) and DRAQ7 (# 424001) were purchased from BioLegend. Anti-mouse CD3 antibody (Clone: KT3) was bought from Bio X Cell.

Synthesis of NIR-IIc PbS/CdS QD—The synthesis of NIR-IIb PbS/CdS QDb can be found in Refence 12. This work developed the synthesis of NIR-IIc PbS/CdS QDc.

The core PbS QD were synthesized using a modified organometallic method[12,26]. In a typical reaction, sulfur precursor solution was prepared by mixing 0.08 g (5 mmol) of sulfur powder, and 7.5 mL of oleylamine in a two-neck flask at 120 °C under argon for 30 min.

Synthesis of PbS quantum dots. 1.668 g (3 mmol) of $PbCl_2$ and 15 mL of oleylamine were mixed in a three-neck flask and degassed for 30 min at 120 °C. The solution was then heated to 165 °C under argon, and kept at that temperature for 15 min. 4.5 mL of the sulfur precursor solution (1.5 mmol of S) was injected into the Pb precursor solution (6 mmol of Pb) under stirring. The temperature was maintained at 165 °C throughout the reaction.

After 180 min, the reaction was quenched by adding 20 mL of cold hexane and 30 mL ethanol. The products were collected by centrifugation and re-suspended in a mixture of 15 mL hexane and 30 mL oleic acid. The quantum dots were precipitated via centrifugation after agitated for 10 min. This precipitation procedure with hexane and oleic

acid was repeated 3 times. The quantum dots were re-suspended in 20 mL toluene after centrifugation.

Synthesis CdS shell on PbS quantum dots. CdO (1.2 g, 9.2 mmol), oleic acid (8 mL), and ODE (20 mL) were mixed in a tree-neck flask and heated to 200 °C for 1.5 hours under argon. The solution was then cooled down to 100 °C and degassed under vacuum for 30 min to afford a Cd precursor solution. 5 mL of the prepared PbS QD suspended in toluene was bubbled with argon for 10 min, and then injected into the Cd precursor solution. The reaction flask was quenched with 5 mL cold hexane after the growth reaction was conducted at 100 °C for 60 min. The PbS/CdS quantum dots were precipitated with ethanol and then re-dispersed in hexane.

Surface modification of PbS/CdS QD with P^3 coating—0.5 mL chloroform solution containing 10 mg PMH was mixed with 2 mg QD dispersed in 0.5 mL cyclohexane. After overnight stirring, the organic solvent was evaporated for 30min by rotary evaporator. The excess residual was heated at 60 °C for 3 hours to fully remove the remaining organic solvent. Afterwards, 1 mL DMAP (10 mg) aqueous solution was added, and the flask was placed in a sonication bath for 10 min to allow the QD to be fully transferred into the water phase. Furthermore, the QD solution was centrifuged at 50000 r.p.m for 2.5 hours. The precipitated were resuspended in 0.5 mL MES (10 mM, pH = 8.5) followed by the addition of 1.5 mg 8Arm-PEG-NH_2·HCl (MW 40k) in 1 mL MES (pH=8.5) and 1 mg EDC. The solution was reacted for 3 hours on orbital shaker. The remaining carboxylic groups were quenched by adding 5 mg Tris-base and 2.5 mg EDC to the above solution. After completion of the reaction for 3 hours, the product was dialyzed against water for 12 hours (300 kDa) to completely remove any by-products. The purification was completed by washing the supernatant with a centrifuge filter tube (100 kDa) and the concentrated sample inside the filter was dispersed in 0.5 mL MES (10 mM, pH = 8.5) solution. 0.5 mg PAA (MW 1800) in 1 ml MES (10 mM, pH = 8.5) together with 1 mg EDC was added and the QD solution was allowed to react for 1 hour. The possible large floccules were removed by the centrifugation of solution at 4400 r.p.m for 30 min, followed by the washing of supernatant by a centrifuge tube (100 kDa) for 4 times. The as-prepared QD@PMH-8ArmPEG-PAA were re-dispersed in 0.5 mL MES solution for final layer coating. As such, the above QD@PMH-8ArmPEG-PAA were mixed with 0.5 mg mPEG-NH_2 (MW 5k), and 0.1 mg 8Arm-PEG-NH_2·HCl (MW 40k) in 1 mL MES solution (10 mM, pH = 8.5). After adding of 1 mg EDC, and the solution was allowed to react for 3 hours. Then, 5 mg Tris-base and 2.5 mg EDC were added into the above solution and left to react for another 3 hours. The reaction product was centrifuged at 4400 r.p.m for 30 min to remove potential large aggregates, then the supernatant was washed by a centrifuge filter (100 kDa) for 4 times. The final QD@PMH-8ArmPEG-PAA-mixed PEG were dispersed in 500 μl 1xPBS solution for further use.

The quantum yield of P^3-QDc was ~ 1.0 % at 808 nm excitation, lower but close to the quantum yield of P^3-QDb (2.6 %) [12] in aqueous solution measured by an integrating sphere as described previously [14].

Conjugation of antibodies on quantum dots

aMECA-79-QDc.: 100-μg MECA-79 antibody was washed by centrifuge filter (10 kDa) for 4 times to remove sodium azide. P^3-QDc (0.25 mg) dispersed in 50 μL 1xPBS solution, MECA-79 antibody (100 μg), EDC (0.6 mg) and 450-μL MES solution (10 mM, pH = 8.0) were mixed and shaken for 3 h. The solution was first centrifuged at 4,400 r.p.m for 30 min to remove potential large floccules. The supernatant was washed by centrifuge filter (10kDa) four times, and then dispersed in 200 μl 1xPBS solution for further intravenous injection.

aCD3-QDc.: P^3-QDc (0.25 mg) dispersed in 50 μL 1xPBS solution, CD3 antibody (200 μg), EDC (0.6 mg) and 450-μL MES solution (10 mM, pH = 8.0) were mixed and shaken for 3 h. The solution was first centrifuged at 4,400 r.p.m for 30 min to remove potential large floccules. The supernatant was washed by centrifuge filter (10kDa) four times, and then dispersed in 50 μl 1xPBS solution for further subcutaneous injection.

aCD169-QDa.: QDa (0.025 mg) dispersed in 50 μL 1xPBS solution, CD169 antibody (50 μg), EDC (0.6 mg) and 450-μL MES solution (10 mM, pH = 8.0) were mixed and shaken for 3 h. The solution was first centrifuged at 4,400 r.p.m for 30 min to remove potential large floccules. The supernatant was washed by centrifuge filter (10kDa) four times, and then dispersed in 50 μl 1xPBS solution for further subcutaneous injection.

NIR-II confocal microscope—A laser beam with wavelength of 808 nm, 1319 nm, 1540 nm or 1650 nm was reflected by a galvo mirror (GVS002, Thorlabs) into a Plössl scan lens (constructed from two achromatic doublets, L3, L4, AC508–150-C, Thorlabs), a Plössl tube lens (constructed from two achromatic doublets, L1, L2, AC508–300-C, Thorlabs) and then focused by an objective into a sample (Supplementary Fig. 3). Fluorescence signal was collected by the same objective, tube lens and scan lens. After de-scanned by the galvo mirror and resized by two achromatic doublets (L5, AC254–100-C and L6, AC508–150-C), the fluorescence light was focused into three single mode (SM) fibers (P1-SMF28E-FC-5, Thorlabs) by achromatic doublets (L7-L9, AC254–030-C, Thorlabs) after filtered by selected emission filters. Then the SM fiber (~ 10 μm mode field diameter) transmitted the fluorescence to NIR-IIb or NIR-IIc SNSPD. The datasheet of P1-SMF28E-FC-5 only gives attenuation data in 1260–1625 nm. We examined the attenuation of this SM fiber in 1000–2000 nm by measuring the emission spectrum of a mixture of three PbS/CdS QDs (emission peaks at 1100 nm, 1340 nm, 1650 nm and 1880 nm respectively) using a spectrometer connected to a 1D extended InGaAs camera (Princeton Instruments) or SNSPD coupled with the SM fiber. The experimental results show the fiber coupled SNSPD has some attenuation as the wavelength longer than 1678 nm, but the attenuation degree is still acceptable for 1200–2000 nm imaging (Supplementary Fig. 4).

For confocal microscopy with PMT (H12397–75, Hamamatsu), a multimode fiber (M122L01, Thorlabs) with core diameter of 200 μm was found necessary to afford sufficient fluorescence signal detectable by the PMT (Supplementary Fig. 11a). We also investigated the fiber effect by imaging blood vessels in mouse stomach in NIR-IIb window ex vivo. Indeed, we found that the 200 μm multimode fiber afforded much higher detection signal than the small 10 μm SM fiber (P1-SMF28E-FC-5, Tholrabs) (Supplementary Fig. 11b–f).

We also compared the sensitivity of PMT and SNSPD by NIR-IIb imaging of a 50 μm capillary embedded in 5% intralipid using the same 1319 nm excitation and ~ 10 μm core single mode fiber as pin-hole. We found that SNSPD allowed a 2.6 mm imaging depth (Fig. 2a), while no signal was detected at an intralipid layer depth of 1.3 mm using PMT (Supplementary Fig. 11a), suggesting the superior sensitivity of SNSPD over PMT.

The galvo mirror, SNSPD and a motorized translation stage (M-VP-25XL, Newport) were synchronized by an acquisition card (NI PCIe-6374) through Labview. This acquisition card also worked as a photon counter to count the TTL signal generated by SNSPD when photons were detected (Supplementary Fig. 3). A 5X objective (NA = 0.12, Leica N Plan), a 10X objective (NA = 0.25, Olympus ULWD MIRPlan), a 20X objective (NA = 0.4, Olympus ULWD MIRPlan), a 20X objective (NA = 0.75, Nikon Plan APO), a 25X objective (NA = 1.05, Olympus XLPLN25XWMP2) and a 100X objective (NA = 0.8, Olympus ULWD MIRPlan) were used in this work. We used heavy water (D_2O) as the immersion liquid for the 25X objective (NA = 1.05) to minimize the absorption by this immersion layer.

For NIR-IIb imaging, longpass filters with a cut-on wavelength of 1500 nm (FELH1500, Thorlabs) or 1580 nm (BLP01–1550R-25) and a bandpass filter (BBP-1530–1730 nm, Spectrogon) were used to generate imaging windows of ~1500–1700 nm or 1580–1700 nm, respectively. For NIR-IIc imaging with 1540 nm excitation, two bandpass filters (FB1750–500 with a transmittance window in 1500–2000 nm and FB2000–500 with a transmittance window in 1750–2250 nm, Thorlabs) were combined for 1750–2000 nm fluorescence collection. For NIR-IIc imaging with 1650 nm excitation, a bandpass filter (FB1900–200 with a transmittance window in 1800–2000 nm was used. A shortpass filter with a cut-off wavelength of 1600 nm (#84–656, Edmund optics) was used to filter 1540 nm laser. For confocal microscopy with 1000–1400 nm emission and 808 nm excitation, a longpass dichroic mirror with cut-on wavelength at 980 nm was used (Di02-R980–25×36, Semrock). For NIR-IIb and NIR-IIc confocal microscopy, longpass dichroic mirrors with cut-on wavelength at 1500 nm and 1800 nm were used, respectively (DMLP1500R, DMLP1800R, Thorlabs).

Resolution analysis—We analyzed the spatial resolution of confocal microscopy with SNSPD by experimental measurements and modeling (see Supplementary Note 3). To estimate the system's best resolution without worsening by scattering, we imaged 300-nm polystyrene beads containing a NIR-II organic dye[20] with different objectives. The nanoparticles were deposited on a coverslip. Fluorescence emission > 1100 nm was collected at 658-nm excitation. The experimental measured FWHM of nanoparticles were consistent well with the FWHM of theoretically calculated point spread function (PSF) along lateral and vertical directions (Supplementary Fig. 12). When a 25X objective (numerical aperture, NA = 1.05) was used, ~ 0.4 μm in lateral and ~ 1 μm in vertical can be achieved. The agreement of experimental data and modeling suggested validity of the analysis for imaging with the organic dyed beads emitting in the 1000–1300 nm range. Due to the lack of beads emitting in NIR-IIc, we only performed modeling and calculated the PSF of confocal microscope in the NIR-IIc window as a function of the pinhole diameter. When a 25X objective (NA = 1.05) and a 1650-nm laser was used, and the fluorescence was collected in NIR-IIc window, the calculated PSF shows FWHMs of ~ 0.83 μm and ~

1.82 μm in lateral and vertical direction, respectively (Supplementary Fig. 13). To estimate the resolution of NIR-IIc confocal microscopy (excitation: 1650 nm; emission: 1800–2000 nm) affected by scattering, we imaged mouse brain with circulating P^3-QDc in blood vessels after sacrificing the mouse, fixation and immersion in 80% glycerol. The measured full width at half maximum (FWHM) of blood vessels were analyzed. The lateral and vertical FWHM of small vessels were ~ 2.0 ± 0.45 μm in lateral and 7.1 ± 0.75 μm in axial directions at depths between 100 μm and 1500 μm in the mouse brain (Supplementary Fig. 14). These corresponded to the lateral and axial resolution limits[1] of NIR-IIc confocal imaging.

Data processing—The raw data of confocal microscopy was processed by a Gaussian filter in ImageJ (1.53c). 3D rendering and multi-color fluorescence image merging were also performed in ImageJ or ImarisViewer 9.6.0 (Oxford Instruments). The FWHM was measured in Origin 9.0. The standard deviation and mean were calculated by Origin 9.0. The PSF was calculated in Matlab (R2019b).

Mouse handling—All procedures performed on the mice were approved by Stanford University's Institutional Animal Care and Use Committee (IACUC). All experiments were performed according to the National Institutes of Health Guide for the Care and Use of Laboratory Animals. The laboratory animal care program at Stanford is accredited by the Association for the Assessment and Accreditation of Laboratory Animal Care (AAALAC). BALB/c female mice were purchased from Charles River. Through this work, we used 3-week-old BALB/c mice (weight: ~ 7 g). The mice were housed on a 12 h: 12 h light: dark cycle (temperature: 20–25 °C, humidity: 50–65 %) in the Stanford University's Veterinary Service Center (VSC), and fed with food and water ad libitum as appropriate. Mice were shaved using hair remover lotion (Nair, Softening Baby Oil). Mice were randomly selected from cages for all experiments. During *in vivo* imaging, all mice were anaesthetized by a rodent anesthesia machine with 2 l min^{-1} O_2 gas mixed with 3 % isoflurane.

In vivo wide-field NIR-II fluorescence imaging—The NIR-II wide-field fluorescence images were recorded by a 2D water cooled InGaAs camera (Ninox640, Raptor Photonics) working at −21 °C. For two-plex imaging, aMECA-79-QDc and p-FE or aCD3-QDc and aCD169-QDa were excited by an 808-nm continuous-wave diode laser. The fluorescence of aMECA-79-QDc and p-FE was collected in 1500–1700 nm and 1200–1400 nm, respectively. The actual excitation intensity was ~ 70 mW cm^{-2}. The fluorescence signal was collected by two achromatic lenses to the camera after filtered by corresponding long-pass and short-pass filters.

In vivo NIR-IIc confocal microscopy of mouse head—To image the blood vessels distribution in mouse head non-invasively (Fig. 3), a 3-week-old BALB/c mouse was intravenously injected with 200 μL NIR-IIb P^3-QDb (O.D. = 5 at 808 nm) and 200 μL NIR-IIc P^3-QDc (O.D. = 5 at 808 nm) sequentially through the tail vein. NIR-IIb and NIR-IIc confocal microscopy was performed 30 min after injection with a 25X objective (NA = 1.05). Detailed experimental conditions are summarized in Supplementary Table 1.

In vivo NIR-IIc confocal microscopy of HEVs in inguinal lymph nodes—For two-color confocal microscopy of HEVs in iLN and blood vessels around the iLN, a 3-week-old BALB/c mouse was first injected with 200 μL aMECA-79-QDc (O.D. = 0.75 at 808 nm) intravenously. 24 h later, 200 μL p-FE (O.D. = 5 at 808 nm) was injected into the tail vein to label the blood vessels. 10 min post injection, two-color NIR-II confocal microscopy was performed. Detailed experimental conditions are summarized in Supplementary Table 1.

In vivo and ex vivo NIR-IIc confocal microscopy of immune cells in inguinal lymph nodes—For two-color confocal microscopy of CD169+ macrophages and CD3+ T cells in iLN, a 3-week-old BALB/c mouse was subcutaneously injected with 50 μL aCD169-QDa (O.D. = 0.3 at 808 nm) and 50 μL aCD3-QDc (O.D. = 3 at 808 nm). 24 hours post injection, two-color NIR-II confocal microscopy was performed. The scan step, dwell time, excitation wavelength filters, and laser powers were summarized in Supplementary Table 1.

After in vivo confocal microscopy, the mouse was euthanized under anesthesia. The iLN was taken out and fixed with 10% neutral-buffered formalin at room temperature for 30 min. Then the iLN was washed by 1X PBS buffer by 3 times and labelled by DRAQ7 for 3 h. After washed in 1X PBS buffer by 3 times, the iLN was preserved in glycerol at 4 °C for ex vivo imaging.

Data availability

Source data are provided with this paper. All data that support the findings of this study are presented in the main text and the Supplementary Information.

Supplementary Material

Refer to Web version on PubMed Central for supplementary material.

Acknowledgments

This study was supported by the National Institutes of Health (NIH DP1-NS-105737, H.D.). We thank Kevin Taylor from JASCO who helped measuring the UV-Vis-NIR absorbance spectrum of water using their V-770 Spectrophotometer. F.R. thanks the Fonds de recherche du Québec – Nature et technologies (FRQNT) for funding (F.R.). Single Quantum acknowledges support from the EIC SME Phase 2 project SQP (848827, R.G., J.W.L., A.F., and J.Q.D.).

References:

1. Horton NG et al. In vivo three-photon microscopy of subcortical structures within an intact mouse brain. Nat. Photonics 7, 205–209 (2013).
2. Yildirim M, Sugihara H, So PTC & Sur M Functional imaging of visual cortical layers and subplate in awake mice with optimized three-photon microscopy. Nature Communications 10, 177 (2019).
3. Kobat D, Horton N & Xu C In vivo two-photon microscopy to 1.6-mm depth in mouse cortex. Journal of Biomedical Optics 16, 106014 (2011). [PubMed: 22029361]
4. Miller MJ, Wei SH, Parker I & Cahalan MD Two-photon imaging of lymphocyte motility and antigen response in intact lymph node. Science 296, 1869–1873 (2002). [PubMed: 12016203]
5. Helmchen F & Denk W Deep tissue two-photon microscopy. Nature Methods 2, 932–940 (2005). [PubMed: 16299478]

6. Svoboda K & Yasuda R Principles of Two-Photon Excitation Microscopy and Its Applications to Neuroscience. Neuron 50, 823–839 (2006). [PubMed: 16772166]
7. Horton NG & Xu C Dispersion compensation in three-photon fluorescence microscopy at 1,700 nm. Biomed. Opt. Express 6, 1392–1397 (2015). [PubMed: 25909022]
8. Wang T et al. Three-photon imaging of mouse brain structure and function through the intact skull. Nature Methods 15, 789–792 (2018). [PubMed: 30202059]
9. Yang Q et al. Donor Engineering for NIR-II Molecular Fluorophores with Enhanced Fluorescent Performance. Journal of the American Chemical Society 140, 1715–1724 (2018). [PubMed: 29337545]
10. Li Y et al. Design of AIEgens for near-infrared IIb imaging through structural modulation at molecular and morphological levels. Nature Communications 11, 1255 (2020).
11. Welsher K et al. A route to brightly fluorescent carbon nanotubes for near-infrared imaging in mice. Nature Nanotechnology 4, 773–780 (2009).
12. Zhang M et al. Bright quantum dots emitting at ~1,600 nm in the NIR-IIb window for deep tissue fluorescence imaging. Proceedings of the National Academy of Sciences 115, 6590–6595 (2018).
13. Bruns OT et al. Next-generation in vivo optical imaging with short-wave infrared quantum dots. Nature Biomedical Engineering 1, 0056 (2017).
14. Zhong Y et al. In vivo molecular imaging for immunotherapy using ultra-bright near-infrared-IIb rare-earth nanoparticles. Nature Biotechnology 37, 1322–1331 (2019).
15. Fan Y et al. Lifetime-engineered NIR-II nanoparticles unlock multiplexed in vivo imaging. Nature Nanotechnology 13, 941–946 (2018).
16. Naczynski DJ et al. Rare-earth-doped biological composites as in vivo shortwave infrared reporters. Nature Communications 4, 2199 (2013).
17. Zhu S et al. 3D NIR-II Molecular Imaging Distinguishes Targeted Organs with High-Performance NIR-II Bioconjugates. Advanced Materials 30, 1705799 (2018).
18. Wang F et al. Light-sheet microscopy in the near-infrared II window. Nature Methods 16, 545–552 (2019). [PubMed: 31086342]
19. Wang F et al. In vivo NIR-II structured-illumination light-sheet microscopy. Proceedings of the National Academy of Sciences 118, e2023888118 (2021).
20. Wan H et al. A bright organic NIR-II nanofluorophore for three-dimensional imaging into biological tissues. Nature communications 9, 1–9 (2018).
21. Golovynskyi S et al. Optical windows for head tissues in near-infrared and short-wave infrared regions: Approaching transcranial light applications. Journal of Biophotonics 11, e201800141 (2018). [PubMed: 30098115]
22. Hong G et al. Through-skull fluorescence imaging of the brain in a new near-infrared window. Nature Photonics 8, 723–730 (2014). [PubMed: 27642366]
23. Burrows PE et al. Lymphatic abnormalities are associated with RASA1 gene mutations in mouse and man. Proceedings of the National Academy of Sciences 110, 8621–8626 (2013).
24. Diao S et al. Fluorescence Imaging In Vivo at Wavelengths beyond 1500 nm. Angewandte Chemie International Edition 54, 14758–14762 (2015). [PubMed: 26460151]
25. Pasko J, Shin S & Cheung D Epitaxial HgCdTe/CdTe Photodiodes For The 1 To 3 pm Spectral Region. Vol. 0282 TSE (SPIE, 1981).
26. Ren F, Zhao H, Vetrone F & Ma D Microwave-assisted cation exchange toward synthesis of near-infrared emitting PbS/CdS core/shell quantum dots with significantly improved quantum yields through a uniform growth path. Nanoscale 5, 7800–7804 (2013). [PubMed: 23887182]
27. Ma Z et al. Cross-Link-Functionalized Nanoparticles for Rapid Excretion in Nanotheranostic Applications. Angewandte Chemie 132, 20733–20741 (2020). [PubMed: 34334834]
28. Zichi J et al. Optimizing the stoichiometry of ultrathin NbTiN films for high-performance superconducting nanowire single-photon detectors. Opt. Express 27, 26579–26587 (2019). [PubMed: 31674536]
29. Wang L, Jacques SL & Zheng L MCML—Monte Carlo modeling of light transport in multi-layered tissues. Comput. Meth. Prog. Bio. 47, 131–146 (1995).

30. Herisson F et al. Direct vascular channels connect skull bone marrow and the brain surface enabling myeloid cell migration. Nature Neuroscience 21, 1209–1217 (2018). [PubMed: 30150661]

31. Pereira ER et al. Lymph node metastases can invade local blood vessels, exit the node, and colonize distant organs in mice. Science 359, 1403–1407 (2018). [PubMed: 29567713]

32. Sewald X et al. Retroviruses use CD169-mediated trans-infection of permissive lymphocytes to establish infection. Science 350, 563–567 (2015). [PubMed: 26429886]

33. Milutinovic S, Abe J, Godkin A, Stein JV & Gallimore A The Dual Role of High Endothelial Venules in Cancer Progression versus Immunity. Trends in Cancer 7, 214–225 (2021). [PubMed: 33132107]

34. Hoshino H et al. Apical membrane expression of distinct sulfated glycans represents a novel marker of cholangiolocellular carcinoma. Laboratory Investigation 96, 1246–1255 (2016). [PubMed: 27748735]

35. Fonsatti E & Maio M Highlights on endoglin (CD105): from basic findings towards clinical applications in human cancer. Journal of Translational Medicine 2, 18 (2004). [PubMed: 15193152]

36. Gaya M et al. Inflammation-induced disruption of SCS macrophages impairs B cell responses to secondary infection. Science 347, 667–672 (2015). [PubMed: 25657250]

37. Girard J-P, Moussion C & Förster R HEVs, lymphatics and homeostatic immune cell trafficking in lymph nodes. Nature Reviews Immunology 12, 762–773 (2012).

38. Gu M, Gan X, Kisteman A & Xu MG Comparison of penetration depth between two-photon excitation and single-photon excitation in imaging through turbid tissue media. Applied Physics Letters 77, 1551–1553 (2000).

39. Hu C, Muller-Karger FE & Zepp RG Absorbance, absorption coefficient, and apparent quantum yield: A comment on common ambiguity in the use of these optical concepts. Limnology and Oceanography 47, 1261–1267 (2002).

40. Wang M et al. Comparing the effective attenuation lengths for long wavelength in vivo imaging of the mouse brain. Biomed. Opt. Express 9, 3534–3543 (2018). [PubMed: 30338138]

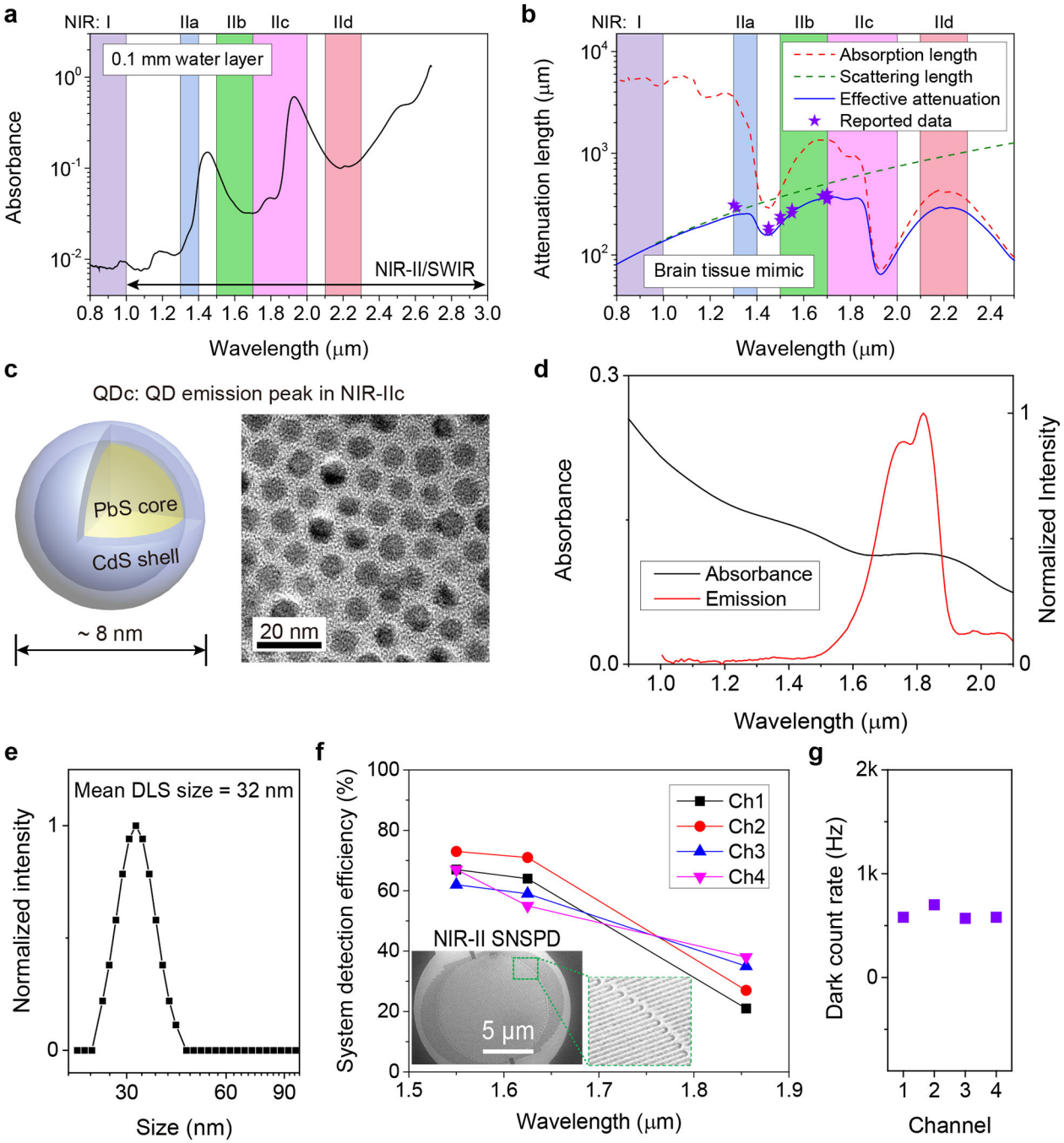

Figure 1 |. Lead sulfide quantum dots and superconducting nanowire single photon detectors enabling fluorescence imaging beyond 1700 nm.

(**a**) The absorbance of water measured in a cuvette with 0.1 mm light path by a spectrophotometer. (**b**) Wavelength-dependent attenuation length ($1/(1/l_s+1/l_a)$) of brain tissue mimicked by 5% intralipid solution. The scattering length (l_s) of mouse brain was mimicked by 5% intralipid solution ($l_s = 0.008\ \lambda^{-2.4}$) [18]. $l_a = 1/\mu_a = L/(D \times \ln 10)$ is the attenuation length of light due to water absorption[39], where μ_a is absorption coefficient, L is optical pathlength and D is absorbance as shown in (**a**). The stars represent previously

reported effective attenuation length of mouse brain measured in vivo[1,40]. (**c**) Schematic design of NIR-IIc core-shell PbS/CdS quantum dots (left) and corresponding transmission electron microscopy (TEM) image (right). Similar TEM results for n = 3 individuals (three batches of new prepared QDc). (**d**) The absorption spectrum of QDc and emission spectrum of P^3-QDc measured in tetrachloroethylene (TCE) or PBS buffer, respectively. A 1-mm cuvette was used. The absorption spectrum was measured in organic phase as the serious absorption of water at ~1445 nm influenced the measurement of absorbance in water. (**e**) Dynamic light scattering spectra of P^3-QDc with polymeric crosslinked network in PBS buffer. (**f**) Optimized multi-channel SNSPD with high system detection efficiency in NIR-IIb (Ch-1and Ch-2) and NIR-IIc (Ch-3and Ch-4) windows. Insets: A scanning electron microscopy image of a typical SNSPD. (**g**) The dark counts of four SNSPD used in our experiments.

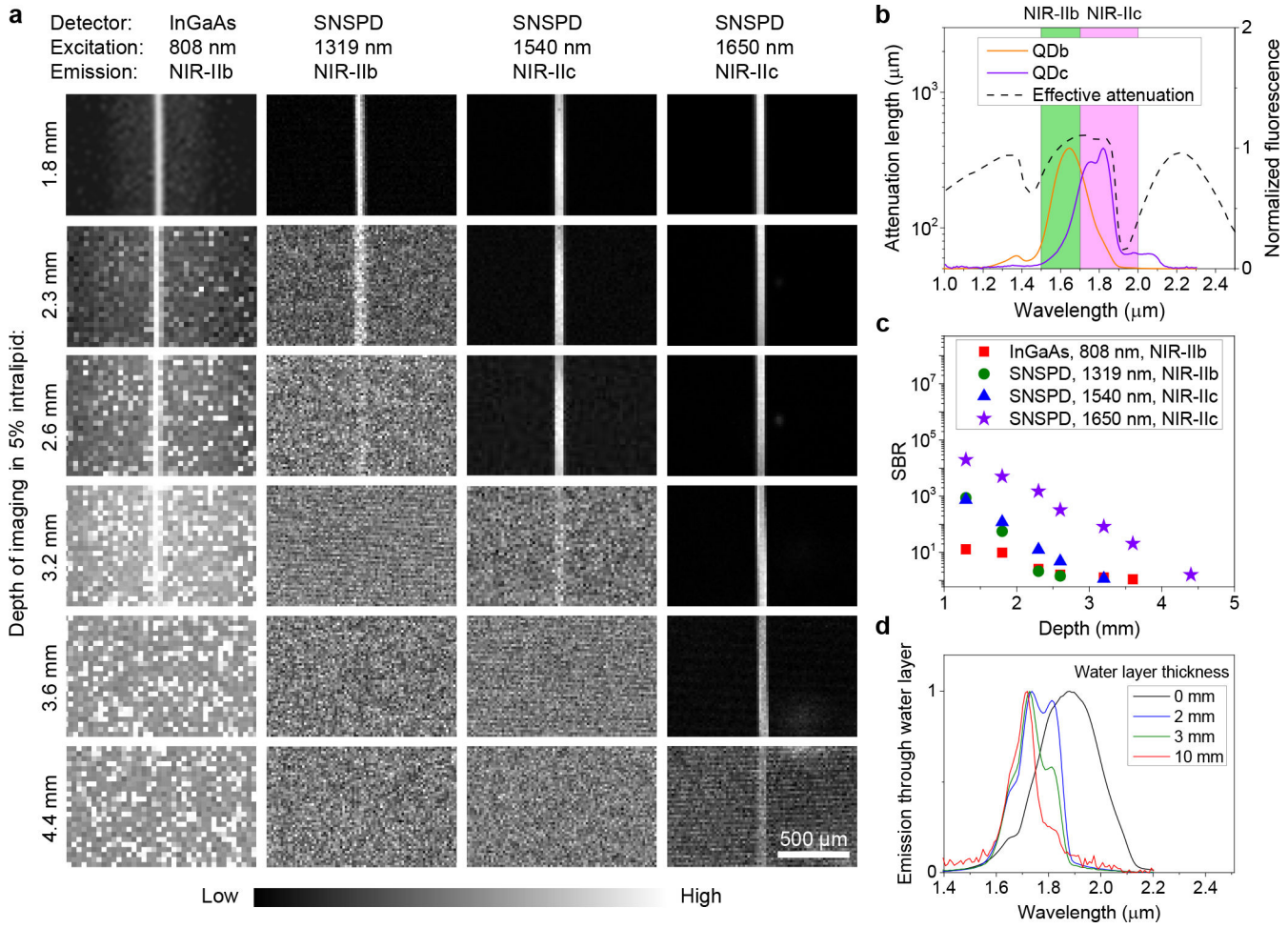

Figure 2 |. Fluorescence imaging in NIR-IIb and NIR-IIc windows.

(**a**) Fluorescence imaging of a 50-μm diameter capillary tube filled with NIR-IIb QDb or NIR-IIc QDc immersed at different depths in 5% intralipid by a wide-field system with a 2D InGaAs camera or a confocal microscope with SNSPDs. The 50-μm diameter capillary tubes immersed in 5% intralipid solution mimicked blood vessels in mouse brain tissues. An 808-nm laser was used for NIR-IIb wide-field imaging. A 1319 nm laser was applied for NIR-IIb confocal microscopy. A 1540-nm laser or a 1650-nm laser and a 10X objective (NA = 0.25) were used for NIR-IIc confocal microscopy. NIR-IIb and NIR-IIc fluorescence was collected in 1500–1700 nm or 1800–2000 nm ranges, respectively. These three lasers had the same power (28.5 mW) at intralipid surface. Similar results for n = 3 individual experiments. (**b**) Fluorescence spectra of P^3-QDb and P^3-QDc in PBS with emission peaks in NIR-IIb [12] and NIR-IIc regions respectively. A cuvette with 1-mm light path was used to measure the spectra. The effective attenuation length is from Fig. 1b. (**c**) Comparison of SBR of the results shown in (**a**). The SBR of wide-field results was from the ratio of the capillary brightness and the signal from sidelobe around the capillary. (**d**) Emission spectra of NIR-IIc QDc in a cuvette measured under water at depths of 2 mm, 3 mm and 10 mm respectively. The 0 mm data indicates no water layer and the emission spectrum was measured with QDc in tetrachloroethylene without any influence from water.

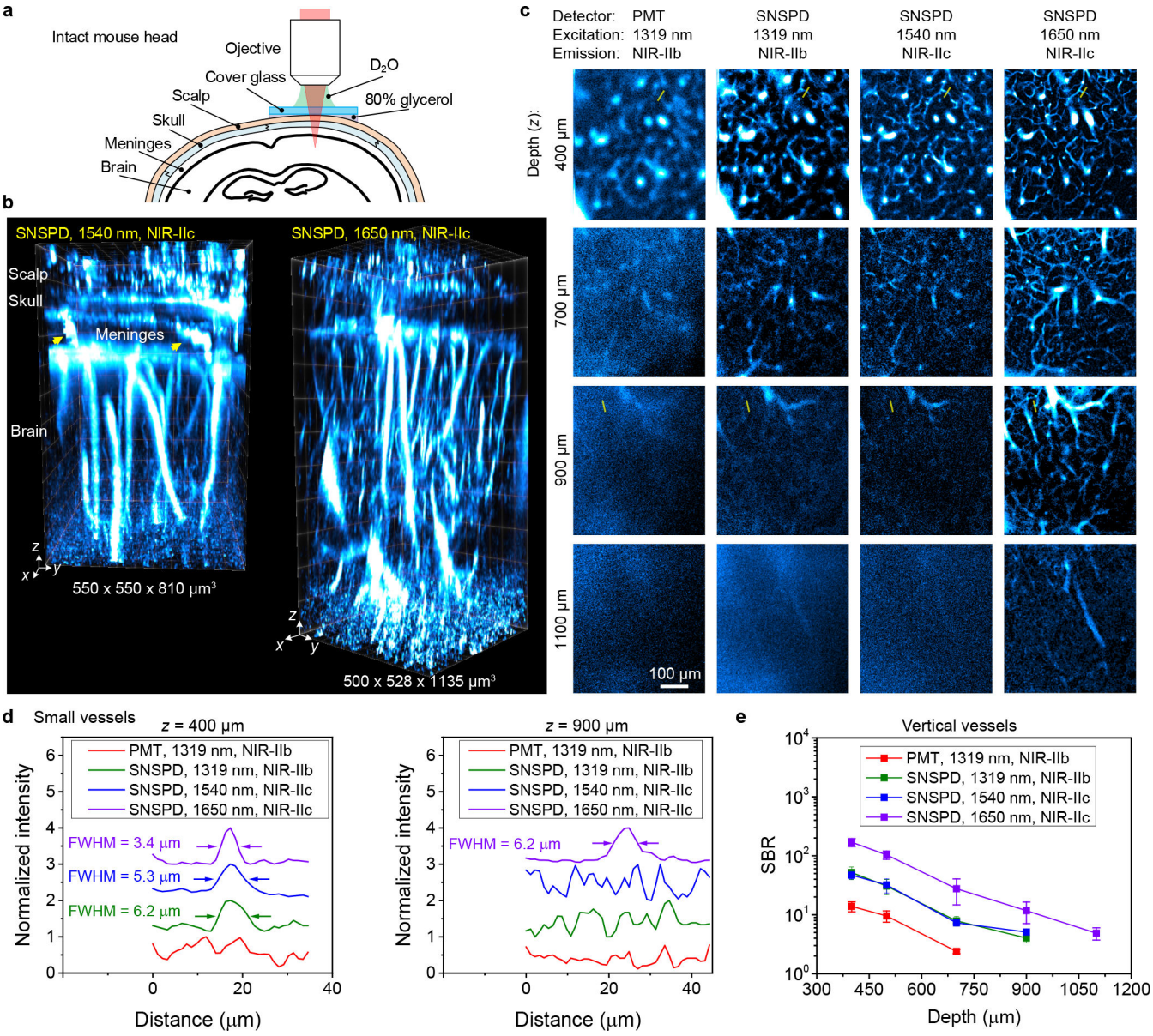

Figure 3 |. Non-invasive *in vivo* confocal microscopy of intact mouse head in NIR-IIc window.

(**a**) Schematic of intact mouse head imaging in NIR-IIc window. The gap between a ~170-μm thick cover glass and mouse head were filled with 80% glycerol. A 25X objective (NA = 1.05) and heavy water (D_2O) as the immersion liquid were used. (**b**) 3D volumetric images of blood vessels in an intact mouse head visualized through the scalp, skull, meninges and brain cortex obtained with a 5-μm *z*-scan increment. The arrows point to the vessel like channels connecting the skull and brain cortex in the meninges. Confocal microscopy was performed 30 min after intravenous injection of P^3-QDc. Left: fluorescence signal was collected in 1750–2000 nm window and excited by a 1540 nm laser. Right: a 1650 nm laser was used and fluorescence was collected in 1800–2000 nm window. (**c**) High-resolution confocal images of blood vessels at various depths through intact mouse head imaged with a PMT or SNSPD in NIR-IIb or NIR-IIc window. Imaging was performed

30 min after intravenous injection of P^3-QDb and P^3-QDc sequentially. NIR-IIb and NIR-IIc fluorescence was collected in 1500–1700 nm and 1800–2000 nm windows and excited by a 1319-nm, a 1540-nm laser and a 1650-nm laser, respectively. These three lasers had the same power (28.5 mW) at mouse head surface. (**b**,**c**) Similar results for n = 3 individuals (BALB/c, female, 3 weeks old). (**d**) Normalized photon counts profiles along the yellow lines in **c**. (**e**) Comparison of SBR for *xy* images recorded at different depths by confocal microscopy with a PMT or SNSPD in different windows. The signals of vertical vessels were used to calculate the SBR as these vessels existed from the surface of brain cortex to the deepest layer of imaging. Data are shown as mean ± s.d. derived from analyzing ≥ 4 vessels at each depth.

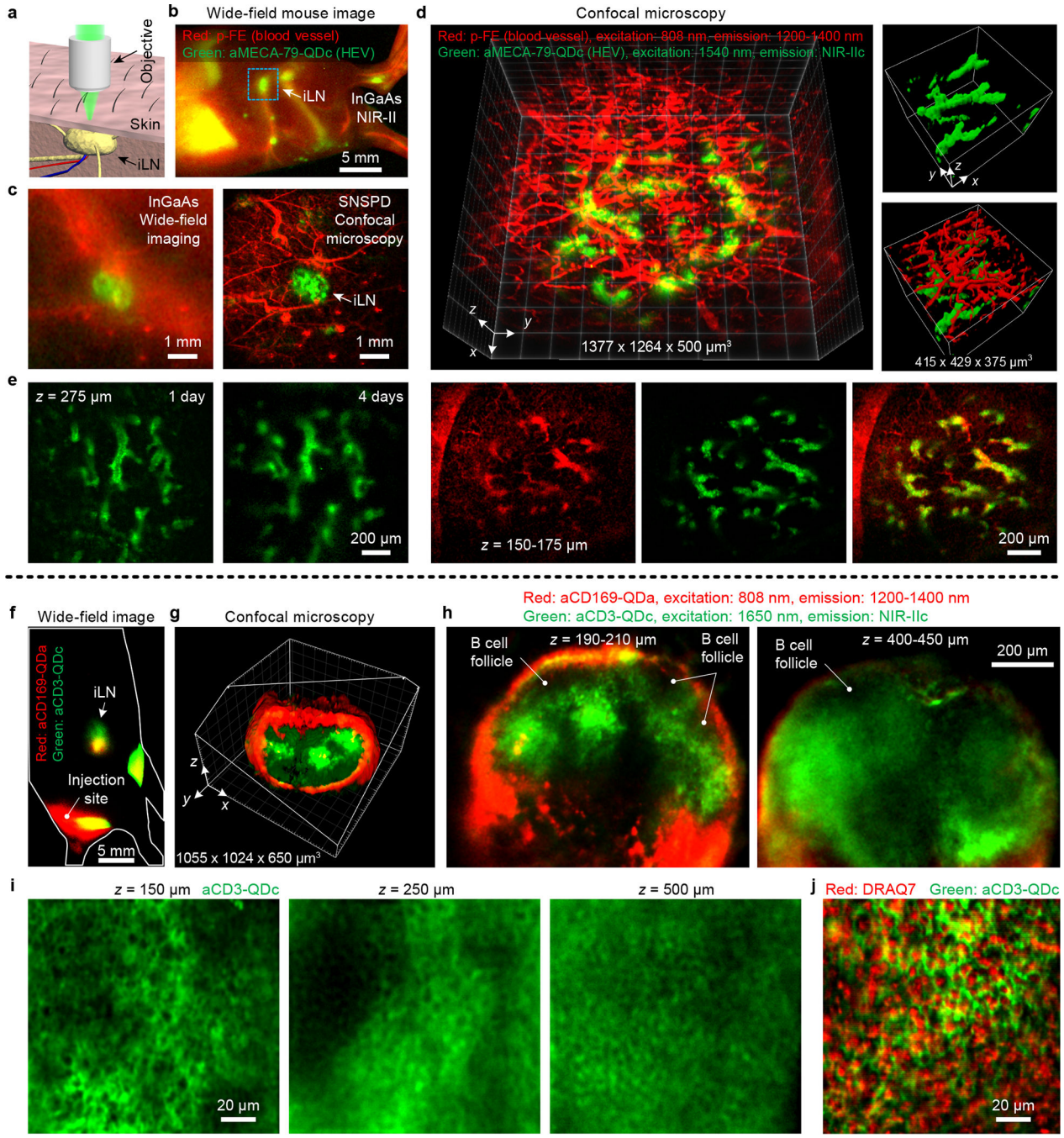

Figure 4 |. Non-invasive *in vivo* NIR-II confocal microscopy of inguinal lymph node in mice.

(**a**) Schematic of non-invasive imaging of iLN by confocal microscope. (**b**) Wide-field imaging of p-FE labelled blood vessels and aMECA-79-QDc labelled HEVs 1 day post intravenous injection of aMECA-79-QDc and 10 min after intravenous injection of free p-FE. (**c**) Comparison of wide-field imaging and confocal microscopy of inguinal lymph node marked by the rectangular in (**b**) at a higher magnification. An 808 nm laser was used for wide-field imaging to excite p-FE and aMECA-79-QDc. For confocal microscopy, p-FE and aMECA-79-QDc were excited by an 808 nm laser and a 1540 nm laser, respectively.

(**d**) Confocal microscopy of blood vessels and HEVs labelled by aMECA-79-QDc in iLN. Skin layer vessels (red) and underlying HEVs (green) in iLN were resolved. (**e**) Longitudinal observation of aMECA-79-QDc labelled HEVs in iLN 1 day and 4 days post intravenous injection. To image the same iLN multiple times, we first located the iLN by wide-field imaging of aMECA-79-QDc. We then focused onto the iLN for confocal microscopy as only the iLN showed strong fluorescence signal due to the antibody-QDc labeled HEVs. (**f**) Wide-field imaging of aCD169-QDa and aCD3-QDc 1 day post subcutaneous injection at the base of tail. (**g**) 3D volumetric imaging of CD169+ macrophages (aCD169-QDa) and CD3+ T cells (aCD3-QDc) in iLN by confocal microscopy of iLN shown in (**f**). (**h**) Maximum-intensity *z*-projections for a 20 μm or 50 μm-thick volume along *z* at $z = 200$ μm and 425 μm, respectively. (**i**) High resolution confocal microscopy of CD3+ T cells in iLN 24 h post subcutaneous injection of aCD3-QDc. (**j**) Ex vivo confocal microscopy imaging of nucleus and CD3+ T cells (aCD3-QDc) in iLN. Similar results for (**b**,**c**,**f**-**j**) n = 3 or (**d**) n = 11 individuals (BALB/c, female, 3 weeks old). Detailed experimental conditions are summarized in Supplementary Table 1.